Chemical Science

ROYAL SOCIETY OF CHEMISTRY

EDGE ARTICLE

View Article Online
View Journal | View Issue

Cite this: *Chem. Sci.*, 2026, **17**, 8028

All publication charges for this article have been paid for by the Royal Society of Chemistry

Heavy-metal free near infrared photoredox catalysts in cancer phototherapy

Mst Nasima Khatun, [a] Satyendu Nandy, [b] Chakali Srinivas, [a] Mrinalini Singh, [a] Ramkrishna Das Adhikari, [c] Sachin Kumar *[b] and Parameswar Krishnan Iyer *[ac]

Herein, five new far red/near infra-red (NIR) heavy-metal free photosensitizers (PSs) were developed by donor modulation of the planar perylenimide (**PI**) core, exhibiting large Stokes shifts of 213–270 nm. The dimethyl-enabled aggregation-induced enhanced emission (AIEE) and tunable AIEE/AIE behaviors of the **RPI** PSs aided precise and efficient superoxide ($O_2^{\bullet-}$) generation for cancer phototherapy, *viz.* **R** = Ph (**PhPI**), $PhNH_2$ (**ANPI**), $PhN(CH_3)_2$ (**DMPI**), −$PhN(Ph)_2$ (TPPI), $PhN(BiPh)_2$ (**BPPI**) to obtain distinct NIR emitters and NIR photoredox catalytic properties. Notably, the solid state NIR emissive **DMPI**, **TPPI** and **BPPI** showed far-red/NIR AIEE, AIE and AIEE behaviors in aqueous media, whereas **PhPI** and **ANPI** displayed aggregation-caused quenching (ACQ) effects. A key discovery is the dimethyl-induced transformation of ACQ-to-AIEE in **DMPI**, enabling a very rare and unusual feature of inducing NIR AIEE properties in the PS. Moreover, the ACQ molecules **PhPI** and **ANPI** generate $O_2^{\bullet-}$/$^{\bullet}OH$ (type-I PS/photoredox) efficiently, **DMPI** exhibits NIR AIEE photoredox characteristics for $O_2^{\bullet-}$ (type-I PS) generation, **TPPI** illustrates far-red AIE photoredox/type-II PS for $O_2^{\bullet-}$/$^1O_2$ (singlet oxygen quantum yield, $\Phi_\Delta = 0.59$ in aqueous media), while **BPPI** demonstrated far-red AIEE photoredox for $O_2^{\bullet-}$ in cancer cells. These systems highlight the diverse optical and therapeutic properties obtained by carefully varying the donor moiety in the **RPIs**. The most prominent dimethyl-induced NIR AIEE design strategy in **DMPI** reveals an exceptional heavy metal-free (NIR AIEE/NIR) photoredox catalyst PS, offering precise and efficient electron transfer for $O_2^{\bullet-}$ production. Importantly, the NIR photoredox catalysts are rarely reported, and the introduction of NIR AIEE photoredox sensitizers expands the scope of current photoredox research. The photocatalytic superoxide generator **TPPI**, developed *via* triplet-ground-state splitting energy modulation, induces significant cancer cell death through a partial O_2-recycling pathway involving Haber–Weiss/Fenton reactions.

Received 7th October 2025
Accepted 23rd February 2026

DOI: 10.1039/d5sc07763j

rsc.li/chemical-science

Introduction

Phototherapy has emerged as a noninvasive alternative, leveraging light-activated PSs to generate ROS, particularly singlet oxygen ($^1O_2$) or type-I radicals ($O_2^{\bullet-}$/$^{\bullet}OH$).[1–3] Type-I phototherapy, favorable for hypoxic tumors, involves electron transfer from the triplet PS to molecular oxygen ($^3O_2$), generating $O_2^{\bullet-}$ through superoxide disproportionation.[4–6] In this photocatalytic strategy, $O_2^{\bullet-}$ is generated upon photon excitation, followed by superoxide dismutase (SOD)-mediated disproportionation and Haber–Weiss/Fenton reactions to produce $^{\bullet}OH$. Through this process, a partial O_2-recycling mechanism is established, enabling sustained oxidative stress and effective cancer cell death.[5,7–9] Herein, the planar **PI** core was selected for its high fluorescence, chemical stability, biocompatibility, and thermal resilience, making it suitable for biomedical applications.[10,11] Despite advances in NIR PS design, particularly donor–acceptor tuning and intersystem crossing (ISC) enhancement, major hurdles still remain due to the detrimental charge transfer characteristics at higher concentrations and the dark toxicity associated with heavy atoms for enhancing spin–orbit coupling (SOC).[8,12,13]

This study introduces a series of five newly synthesized peri-functionalized **PI** based PSs with unique photophysical properties, biocompatibility, and remarkable chemical and thermal stability, making them suitable for therapeutic and clinical applications.[10,11] These five PSs include **RPI** [2-hexyl-8-phenyl-1*H*-benzo[5,10]anthra[2,1,9-def]isoquinoline-1,3(2*H*)-dione (**PhPI**)/8-(4-aminophenyl)-2-hexyl-1*H*-benzo[10,5]anthra[2,1,9-def]isoquinoline-1,3(2*H*)-dione (**ANPI**)/8-(4-(dimethylamino)phenyl)-2-hexyl-1*H*-benzo[10,5]anthra[2,1,9-def]isoquinoline-1,3(2*H*)-dione (**DMPI**)/8-(4-(diphenylamino)phenyl)-2-hexyl-1*H*-benzo[10,5]anthra[2,1,9-def]isoquinoline-1,3(2*H*)-dione (**TPPI**)/8-(4-(di([1,1′-biphenyl]-4-yl)amino)phenyl)-2-hexyl-1*H*-benzo[10,5]anthra[2,1,9-def]isoquinoline-1,3(2*H*)-dione (**BPPI**)], each possessing donor functionality with minor variations, attached to the **PI** core (Fig. 1). These **RPI** PSs were carefully designed and

[a]*Department of Chemistry, Indian Institute of Technology Guwahati, Guwahati-781039, India. E-mail: pki@iitg.ac.in; Fax: +913612582349*

[b]*Department of Bioscience and Bioengineering, Indian Institute of Technology Guwahati, Guwahati-781039, Assam, India*

[c]*Centre for Nanotechnology, Indian Institute of Technology Guwahati, Guwahati-781039, India*

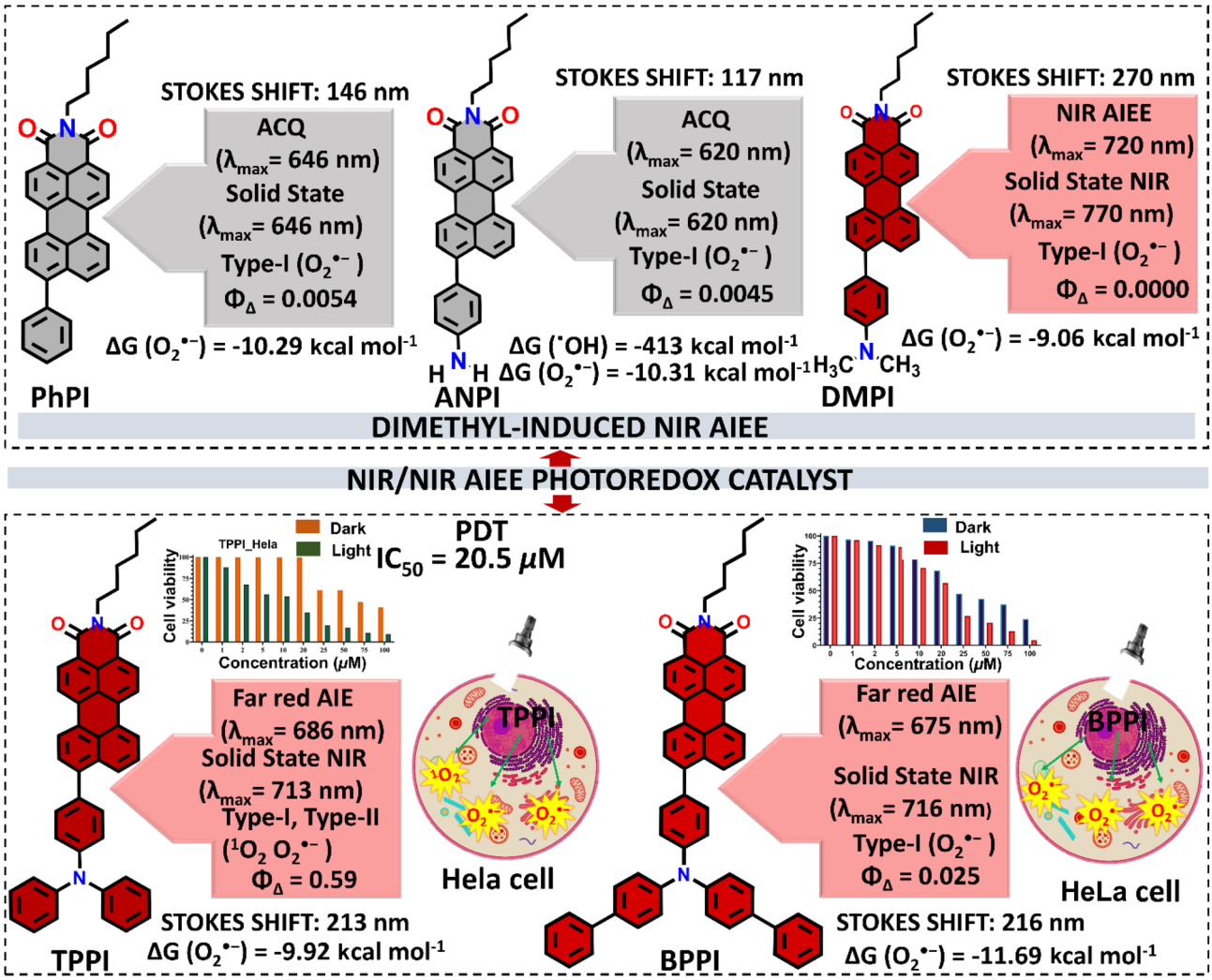

Fig. 1 The graphical representation of various **RPIs** illustrates far-red/NIR condensed state emitters, large Stokes shift (213–270 nm) tuning, and NIR/NIR AIEE photoredox catalytic activity for $O_2^{\bullet-}$ generation and diverse PS functionalizations (type-I/dual type/type-II) for cancer phototherapy ($IC_{50} = 20.5$ μM). The graphic represents dimethyl-induced NIR AIEE behavior, and highlights a triplet-ground-state splitting modulation strategy that enables a partial O_2-recycling mechanism, where $O_2^{\bullet-}$ drives Haber–Weiss/Fenton reactions that could be applicable for effective cancer cell death even under hypoxia (≤2% O_2).

synthesized to modulate diverse properties, including far-red/NIR AIE/AIEE, higher Stokes shift in the range of 213–270 nm, distinct PS (type-I/dual type/type-II), and precise (NIR AIEE/NIR) photoredox catalysts that produce various ROS ($^{\bullet}OH/O_2^{\bullet-}$). This work conceptualizes unique dimethyl-induced NIR AIEE characteristics in the planar **PI** core that arise from steric crowding around the pendant phenyl unit, which transforms ACQ into AIEE features in **DMPI**. Thus, **DMPI** demonstrated NIR AIEE photoredox catalytic properties ($O_2^{\bullet-}$, type-I PS) while **TPPI** exhibited type-II PS behavior and Φ_Δ of 0.59 in aqueous media. **TPPI** and **BPPI** PSs exhibited solid state NIR emission, while **TPPI** showed dual type PS/photoredox ($^1O_2$ and $O_2^{\bullet-}$) behavior and **BPPI** was a type-I ($O_2^{\bullet-}$) PS/photoredox catalyst for effective cancer phototherapy. This work also hypothesized the ground-triplet state splitting energy for meticulous NIR photoredox catalyst formulation. Thus, this approach offers for the first time a promising platform for the development of heavy-metal-free design principles for advancing distinct (NIR/NIR AIEE) photoredox systems that generate precise ROS ($O_2^{\bullet-}$). Additionally, this work also revealed a unique dimethyl-induced effect in NIR AIEE design that enabled diverse structure based optical tuning (Fig. 1 and Tables S1, S2). Notably, while NIR photoredox catalysts are rare, the development of NIR AIEE photoredox catalysts represents a significant conceptual advancement. **TPPI** is designed *via* an intramolecular triplet-ground-state splitting energy modulation strategy; it functions through a partial O_2-recycling mechanism in which $O_2^{\bullet-}$ drives Haber–Weiss/Fenton reactions, enabling effective cancer cell death.

Results and discussion

Design, synthesis, and characterization of RPIs

This study explores the condensed state optical and NIR photoredox catalytic properties of novel **RPIs** with minor donor unit variation at the peri-position of the acceptor **PI** core, *viz*, **RPI: PhPI**/

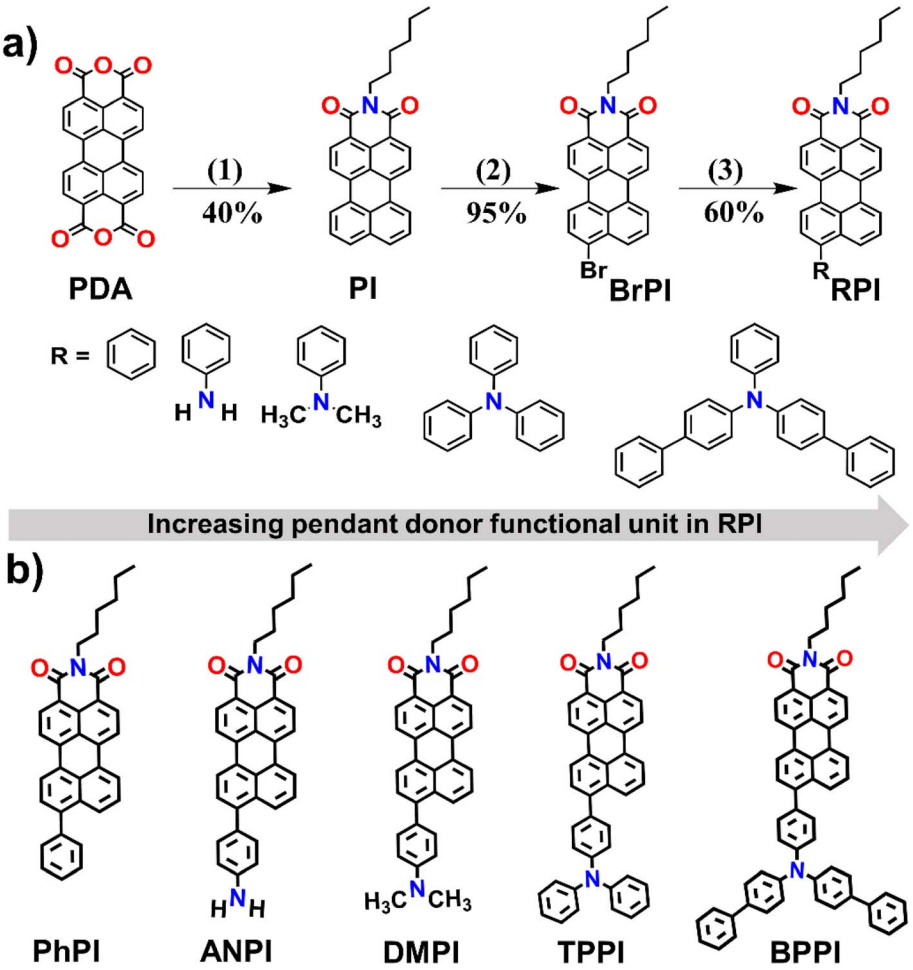

Scheme 1 (a) Synthetic method employed for preparing RPIs (PhPI/ANPI/DMPI/TPPI/BPPI) with increasing donor unit at the peri-position of the PI core. (b) Chemical structures of the synthesized RPIs [(1) hexyl amine, H_2O, 20 h, (2) chlorobenzene, Br_2, 4.5 h, (3) Pd (0), THF/H_2O, values below the arrow are the yields of corresponding products].

ANPI/DMPI/TPPI/BPPI, that have been carefully synthesized from PDA *via* hexylamine condensation, bromination, and Suzuki coupling with good yields. Detailed synthetic procedures and characterization data are provided in Schemes 1 and S1–S3 (SI).

Photophysical behaviors

The optical properties of the newly designed **RPIs** were investigated using UV-vis absorption and photoluminescence (PL) spectroscopy in solution (DMSO), aggregated (DMSO/H_2O) and solid states (Fig. 2 and Tables 1, S3). The absorption spectra revealed that increasing the donor functional unit in the peri-position significantly influenced π-conjugation within the **PI** core (Fig. 2a and Table 1). Among them, **ANPI** (absorption maxima, $\lambda_{abs,max}$ = 550 nm)/**DMPI** ($\lambda_{abs,max}$ = 550 nm) exhibited a 30/50 nm red-shifted $\lambda_{abs,max}$ due to their enhanced delocalization, compared to **PhPI** ($\lambda_{abs,max}$ = 500 nm). Further increasing the donor unit at **RPI**, *viz.* **TPPI** ($\lambda_{abs,max}$ = 527 nm)/**BPPI** ($\lambda_{abs,max}$ = 525 nm) exhibited a 23/25 nm blue shifted $\lambda_{abs,max}$ relative to **DMPI**. This peculiar shift is attributed to reduced electronic communication, likely due to their steric hindrance and spatial separation of the HOMO/LUMO, as supported by further DFT analyses. Corresponding emission maxima ($\lambda_{em,max}$) showed trends consistent with $\lambda_{abs,max}$. **ANPI** ($\lambda_{em,max}$ = 603) exhibited a 42 nm red-shifted $\lambda_{em,max}$, compared to **PhPI** (Fig. 2b, b′ and Tables 1, S3). **DMPI** ($\lambda_{em,max}$ = 588 nm) showed less pronounced $\lambda_{em,max}$, while **TPPI/BPPI** demonstrated 42/39 nm blue shifted $\lambda_{em,max}$ compared to **PhPI**, despite having stronger donor units. This inconsistency suggests reduced electronic communication in the solution state. The solution state $\lambda_{em,max}$, spanning yellow-green to red, has been presented in the CIE chromaticity diagram (Fig. 2b′ and Table S3). However, **RPIs** demonstrated prominent red-shifted $\lambda_{em,max}$ of ∼100/150 nm in their aggregated/solid state (Fig. 2c, d, and Table 1). **DMPI** displayed NIR $\lambda_{em,max}$ at 720/770 nm in its aggregated/solid state, which arises from its effective molecular packing. **TPPI/BPPI** exhibited far-red/NIR $\lambda_{em,max}$ at 686/713 nm and 675/716 nm, respectively, in their aggregated/solid state. The CIE plot exhibited far-red/NIR colors in the aggregated-state (Fig. 2c′, d′ and Tables 1, S3). **DMPI/TPPI/BPPI** showed significant 50/27/41 nm red-shifted $\lambda_{em,max}$ in their solid state compared to the aggregated state due to their distinct molecular arrangements (Fig. 2e and Table 1). In contrast, **PhPI/ANPI** showed minimal shifts in their condensed

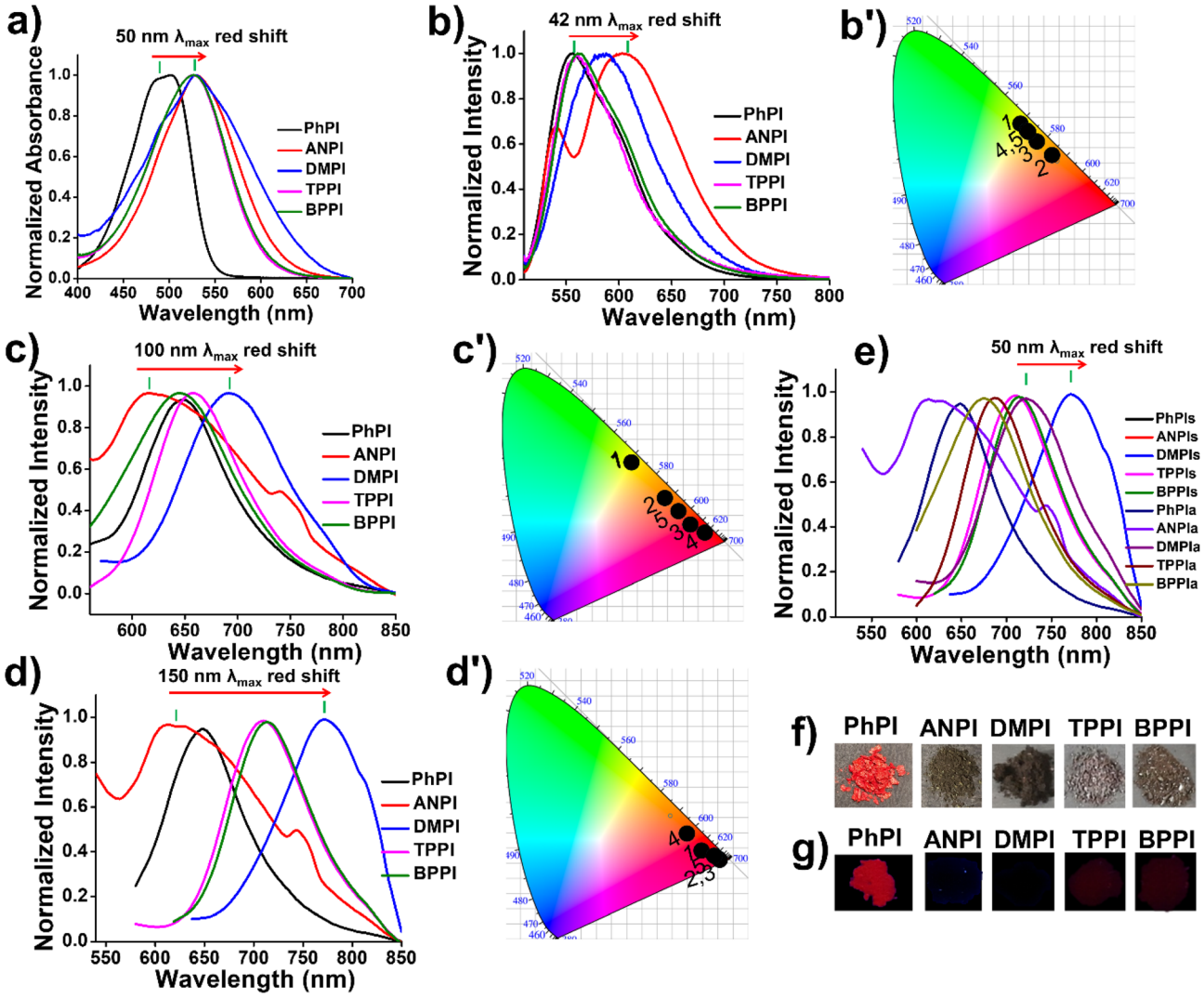

Fig. 2 Photophysical properties of the RPIs (PhPI/ANPI/DMPI/TPPI/BPPI): (a) normalized UV-vis absorbance spectra in DMSO (solution state, 100 μM). (b) PL spectra of RPIs in solution state. (b′) CIE chromaticity diagram for solution state fluorescence color. (c) Normalized PL spectra at 99% f_w in DMSO. (c′) CIE coordinates in the aggregated state. (d) Solid state normalized PL spectra. (d′) CIE chromaticity diagram for solid state emission color. (e) Comparison of PL spectra in aggregated and solid states. (f and g) Digital photographs of the solid RPIs in powder form under daylight and UV excitation (λ_{ex} = 500 nm). [a and s: aggregated and solid state, respectively; λ_{ex} = 500 nm. Inset in CIE: 1–5 = PhPI/ANPI/DMPI/TPPI/BPPI].

state, indicating stable conjugation. This distinct molecular arrangement was further analyzed using excitation-emission matrix (EEM) spectroscopy. Under white light and 365 nm UV illumination, visible appearance differences in powder form were observed. **PhPI**/**ANPI** appeared colorless due to their non emissive nature, while **DMPI** also lacked visible color owing to its NIR emission, that requires NIR excitation. **TPPI**/**BPPI** showed a distinct far-red color optical appearance (Fig. 2f and g).

Thus, by varying the donor units, the $\lambda_{em,max}$ trend remained unaffected by the electronic properties of these functional units in their aggregated/solid state. This highlights that AIE properties are governed by functional units, suggesting that condensed state photophysical properties are independent of electronic effects.[14–16] The functional units play pivotal roles, exerting varying steric constraints on the parent **PI** core, thereby manipulating its molecular organization and resulting in distinct condensed state emitters. Moreover, the **RPIs** exhibited exceptional Stokes shifts (117–270 nm), surpassing the widely used isoquinoline-based analogs like **IQ-TPA** (173 nm) and **TPE-IQ-TPA** (212 nm).[17,18]

ACQ to far-red/NIR AIE/AIEE transformation

To investigate the aggregation properties of the **RPIs**, UV-vis, and PL spectra were measured in 99% water fractions (f_w) (Fig. 3, S1–S13 and Tables 1, S1–S10). At 0% f_w, **ANPI**/**DMPI**/**TPPI**/**BPPI** displayed $\lambda_{abs,max}$ at 530/550/527/525 nm, respectively, corresponding to π–π* transitions (Fig. S2, S3, and Table S4). **PhPI** showed two characteristic peaks at 483/500 nm, indicating π–π* and intramolecular charge transfer (ICT) from phenyl donor to the acceptor **PI** core. Furthermore, solvent polarity-dependent PL

Table 1 Summary of the photophysical and PS/photoredox catalytic information of the RPIs

Photosensitizers	$^{a}\lambda_{abs}$ (nm)	$^{a}\lambda_{ex}$ (nm)	$^{a}\lambda_{em}$ (nm)	$^{b}\lambda_{em}$ (nm)	$^{b}\lambda_{em}$ (nm)	^{c}Stokes-shift (nm)		$^{d}\Phi_{PL}$	$^{e}E_g$ (eV)	$^{f}\Phi_{\Delta}$	$^{g}\Delta E_{S_1-T_1}$ (eV)	^{h}SOC (cm^{-1})	$\Delta E_{S_0-T_1}$ (eV)
						$A-E$	$S-E$						
PhPI	500	500	580	646	646	146	146	0.0387	2.66	0.0054	1.182	0	1.165
ANPI	530	500	603	620	620	117	117	0.0693	2.566	0.0045	1.083	0	1.079
DMPI	550	500	588	720	770	220	270	0.196, 0.044[p]	2.480	*g*	0.623	0.447	1.002
TPPI	527	500	561	686	713	186	213	0.0534, 0.098[p]	2.410	0.592	0.639	0.141	2.532
BPPI	525	500	564	675	716	175	216	0.033, 0.0999[p]	2.340	0.025	0.522	0.141	0.871

[a] $\lambda_{ab,max}$, λ_{ex} and $\lambda_{em,max}$ represent absorption, excitation, and emission wavelength maxima, respectively, in the solution state. [b] Aggregated and solid state $\lambda_{em,max}$. [c] Stokes-shift calculated between the aggregated-state $\lambda_{em,max}$ and λ_{ex} ($A-E$), whereas ($S-E$) represents the Stokes-shift between the solid state $\lambda_{em,max}$ and λ_{ex}. [d] Φ_{PL} indicates the PL quantum yield in the aggregated state. [e] E_g demonstrates gaseous-state band-energies. [f] Φ_{Δ} represents the singlet-oxygen quantum yield. [g] ΔE_{ST} is the first singlet and triplet state energy gap. [h] SOC between the singlet and triplet states. [p = Φ_{PL} at 60% f_w]. $\Delta E_{S_0-T_1}$ is the intramolecular triplet-ground state splitting energy. g = not observed.

studies confirmed ICT nature in the **RPIs** (Fig. S5 and Tables S7, S8). **DMPI** exhibited a more pronounced ICT effect, comprising 38/56 nm red-shifted $\lambda_{abs,max}/\lambda_{em,max}$, respectively, while **TPPI**/**BPPI** showed 12/49 and 10/38 nm red-shifted $\lambda_{abs,max}/\lambda_{em,max}$ in polar solvents, respectively. At 99% f_w, **PhPI**/**ANPI** exhibited prominent ~70/73 nm blue shifted $\lambda_{abs,max}$ due to H-aggregation energized by pronounced π–π stacking of the acceptor **PI** core (Tables S4 and S5). Conversely, **DMPI** exhibited 10 nm red-shifted $\lambda_{abs,max}$ (J-type aggregation). Importantly, **TPPI**/**BPPI** showed distinct spectral shifts at 99% f_w. This peculiar spectral behavior observed in the concentration-dependent studies in DMSO (100 μM–1 mM), revealed stable $\lambda_{abs,max}$ for **PhPI**/**ANPI**, whereas **DMPI**/**TPPI**/**BPPI** exhibited 12/1/3 nm red-shifted $\lambda_{abs,max}$ (J-type aggregation) (Fig. S4 and Table S6). At 0% f_w, **PhPI**/**ANPI**/**DMPI**/**TPPI**/**BPPI** showed corresponding $\lambda_{em,max}$ at 580/603/588/561/564 nm, respectively (Fig. 3 and S1). At 99% f_w, **PhPI**/**ANPI** showed ACQ behavior consisting of quenched and red-shifted $\lambda_{em,max}$ at 646/620 nm (Fig. 3a–a″, S1 and Table 1). Although **DMPI**/**TPPI**/**BPPI** showed less pronounced or blue shifted $\lambda_{em,max}$ compared to **PhPI**/**ANPI**, **DMPI** exhibited NIR AIEE features ($\lambda_{em,max}$ = 720 nm) while **TPPI**/**BPPI** displayed far-red AIE/AIEE characteristics ($\lambda_{em,max}$ = 686/675 nm) (Fig. 3b–b″, c–c″, d–d″ and Table 1). The distinct H- and J-aggregation behaviors observed for these **RPI** derivatives can be rationalized based on Kasha's exciton coupling model for one-dimensional molecular assemblies, in which positive and negative excitonic coupling lead to blue- and red-shifted optical spectra relative to the monomer, corresponding to H- and J-aggregates. Small organic chromophores typically form H- or J-type aggregates depending on the relative orientation of their transition dipole moments, and the aggregation mode strongly governs the position and shape of their absorption bands. Compared with isolated monomers in the diluted solution, a hypsochromic (blue) shift is characteristic of H-aggregation arising from cofacial π–π stacking, whereas a bathochromic (red) shift indicates J-aggregation associated with slipped or head-to-tail molecular arrangements.[19,20] In H-aggregates, positive coulombic (exciton) coupling produces a manifold of excited states in which the highest energy state carries most of the oscillator strength. Because fluorescence typically occurs from the lowest excited state (Kasha's rule), radiative decay is suppressed in H-aggregates, favoring non-radiative pathways such as internal conversion and intersystem crossing.[21] In contrast, J-aggregates are characterized by negative excitonic coupling that concentrates oscillator strength in the lowest-energy exciton state, thereby preserving or even enhancing fluorescence. Consequently, controlling the aggregation mode provides an effective strategy to tune the photophysical and electronic properties of organic semiconductors.[19,20,22,23] In this context, **PhPI** exhibits H-type aggregation, as evidenced by its pronounced blue shifted $\lambda_{abs,max}$ (Fig. S3 and Tables S4, S5). In contrast, although **BPPI** displays invariant $\lambda_{abs,max}$ at a lower concentration, it shows J-type aggregation behavior, as supported by concentration-dependent UV-vis absorption studies in both mixed solvents and DMSO (Fig. S3, S4 and Tables S4, S6). Specifically, in DMSO (100 μM–1 mM), **PhPI** shows an almost invariant $\lambda_{abs,max}$, whereas **BPPI** exhibits a gradual red shift of approximately 3 nm, consistent with J-aggregate formation

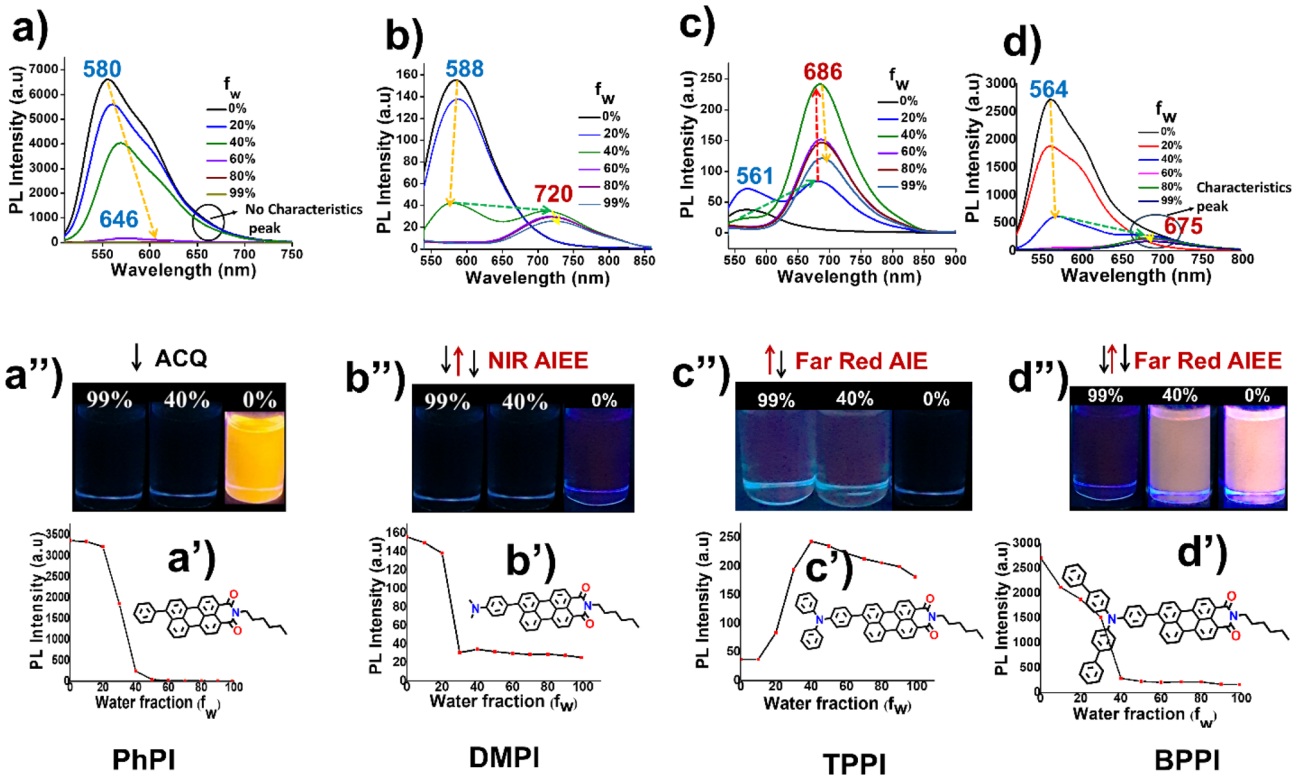

Fig. 3 PL spectra of (a) **PhPI**, (b) **DMPI**, (c) **TPPI**, and (d) **BPPI**, at different f_w in DMSO (100 μM, $\lambda_{ex} = 500$ nm). (a′–d′) Plots of $\lambda_{em,max}$ at various f_w along with insets: (a″–d″) digital photographs under 365 nm UV irradiation of the corresponding **RPI** at 0/40/20/99% f_w in DMSO with their corresponding chemical structures [daylight photographs of all the **RPIs** have been placed in Fig. S11 in the SI].

(Fig. S4, and Table S6). These distinct spectral features highlight the fundamentally different aggregation modes of **PhPI** and **BPPI**, which has been further confirmed by the characteristic peak appearance for **BPPI** upon aggregation (Fig. 3a and d). Although **TPPI** exhibits a 27 nm blue shifted $\lambda_{abs,max}$, its J-aggregation is indicated by a 1 nm red-shifted $\lambda_{abs,max}$ UV peak at higher concentrations, which subsequently leads to its promising characteristic peak appearance at 686 nm upon aggregation (Fig. 3c). In the present system, strong π–π interactions of the electron acceptor **PI** core promote H-type aggregation (Fig. S3 and Tables S4, S5). However, **DMPI** exhibits a distinct approximately 10/12 nm red-shifted $\lambda_{abs,max}$ both at lower and higher concentrations, indicating a more prominent J-type aggregation character (Fig. S3, S4 and Tables S4, S6). This J-type packing mitigates the fluorescence quenching typically induced by strong π–π stacking of the **PI** core and, together with restriction of intramolecular rotation (RIR), leads to enhanced emission in the aggregated-state. The extent of J-aggregation among **DMPI**, **TPPI**, and **BPPI** follows the order **DMPI** > **BPPI** > **TPPI**, as reflected by their respective bathochromic $\lambda_{abs,max}$ shifts of approximately 12, 3, and 1 nm in the aggregated state (considering the UV-vis spectra at higher concentrations as aggregation is the concentration dependent phenomenon, and likely affects the UV-vis spectra by involving aggregated molecules) (Fig. S4 and Table S6).[15] This trend can be attributed to the steric and conformational effects of the donor units attached to the **PI** core. In **DMPI**, the flexible donor moiety enables greater segmental motion and closer intermolecular association, leading to aggregation-induced red-shifted emission and pronounced NIR AIEE behavior. In contrast, the bulkier donor units in **TPPI** and **BPPI** restrict segmental motion and hinder effective aggregation, thereby suppressing large spectral red shifts and resulting in far-red AIE/AIEE emission. Previous studies have shown that solvent polarity and aggregation strongly influence the emission behavior of donor–acceptor luminogens.[24–30] Interestingly, For **BPPI**, the $\lambda_{em,max}$ is observed at 564 nm in pure DMSO (0% f_w). As solvent polarity increases, the twisted ICT (TICT) state stabilizes, resulting in a red shift and a decrease in emission intensity up to 40% f_w. Beyond this critical point, molecular aggregation restricts intramolecular motion and suppresses TICT formation, consequently, emissive J-type aggregates dominate the photophysical behavior with a new characteristic peak at 675 nm (far-red AIEE) (Fig. 3d–d″).[14] The decline of $\lambda_{em,max}$ after aggregation was due to its agglomeration.[31] Furthermore, the AIE/AIEE behavior of all the molecules was estimated by correlating PL photographs, and PL intensity *versus* f_w profiles.[14] Herein, **PhPI** and **ANPI** exhibited typical ACQ properties, as evidenced by decreased emission upon aggregation. In contrast, **DMPI**, **TPPI**, and **BPPI** displayed AIEE/AIE characteristics. When molecularly dispersed in DMSO, the luminophores are weakly or moderately emissive, and as the f_w increases, emission initially decreases due to enhanced TICT formation. Beyond a critical f_w, aggregation occurs and the RIR suppresses the nonradiative decay pathway, promoting radiative relaxation and resulting in enhanced emission. In solution,

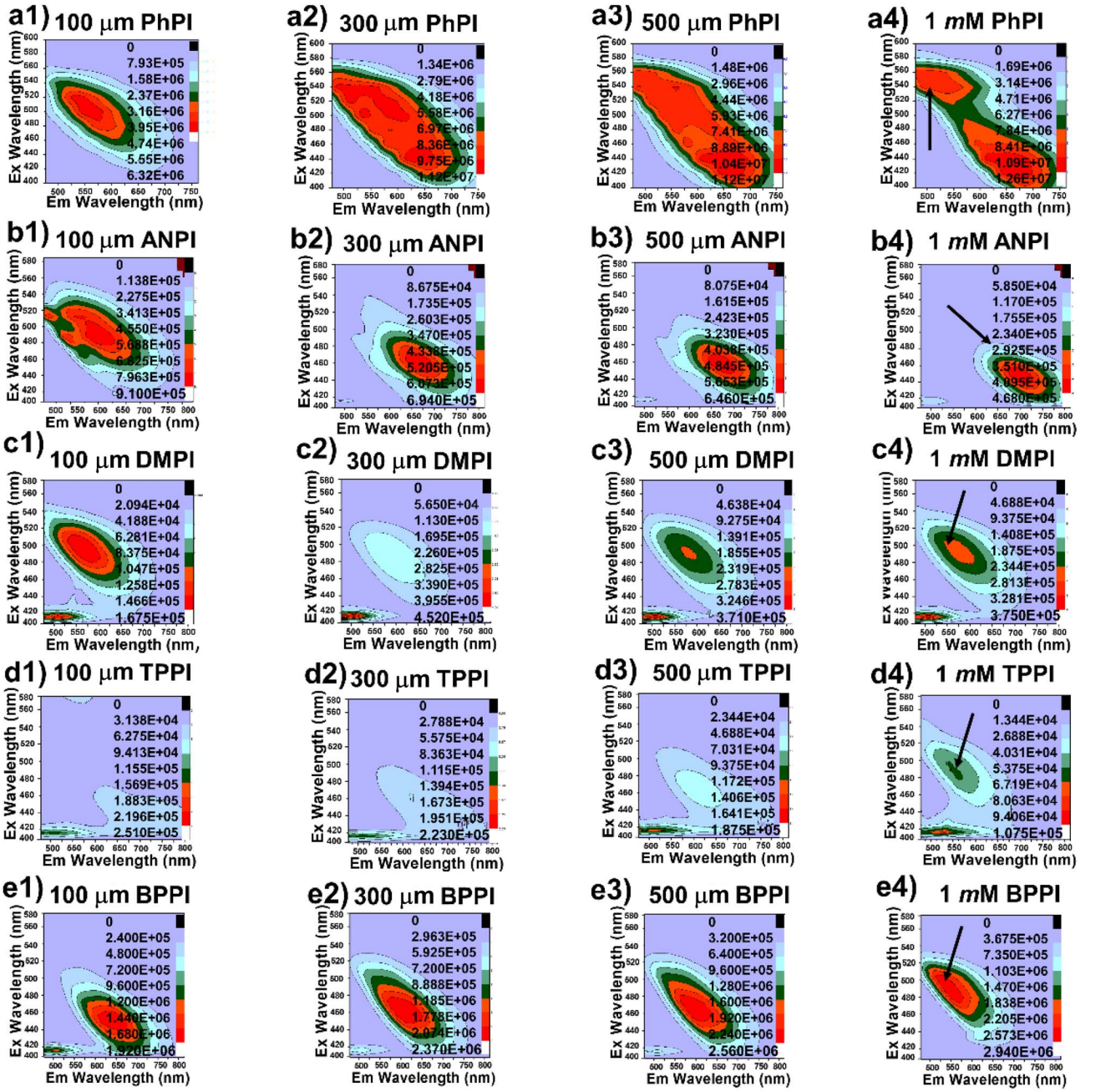

Fig. 4 (a1–e4) 2D EEM contour plots of the RPIs from lower to higher concentrations (left: 100 μM; middle: 300 μM and 500 μM; right: 1 mM) in DMSO [inset: arrow signifies the PL intensity].

fluorescence is mainly governed by the rotational motion of the functional groups appended to the core, energized by their diverse electronic effects, whereas in the aggregated or solid state, intermolecular steric effects hinder these motions and favor radiative decay pathways (Fig. 3).[15,32] Interestingly, **BPPI** exhibits weak red emission in the solid state, despite showing strong emission in DMSO (Fig. 2g and 3d″). As shown in Fig. 2f and g, **BPPI** displays red emission in the solid state under 365 nm UV irradiation, which is distinctly different from its appearance under daylight. However, the solid-state emission is relatively weak, which can be attributed to its inefficient intermolecular packing interactions arising from the steric constraints imposed by the attached bulkier functional units on the parent **PI** core. In contrast, the strong emission observed in DMSO originates from the promising electronic effect of the appended group when the **BPPI** molecules are in an isolated state. The solid-state emission governed by the restricted packing and solution state emission dominated by intrinsic electronic transitions are consistent with previously reported luminogens.[15,16,32] More interestingly, **PhPI** exhibits red emission in the solid state and yellow emission in DMSO; however, it becomes non-emissive upon aggregation (Fig. 2g and 3a–a″). The solution state emission of **PhPI** arises

due to its unique electronic constraints of the appended unit, where molecules are in a totally dispersed state. In the solid state, restricted intramolecular motion partially suppresses non-radiative decay pathways, leading to red emission. In contrast, in the aggregated-state, strong π–π stacking interactions between planar **PhPI** molecules facilitate exciton coupling and promote nonradiative relaxation pathways that could be due to its excited state planarity and increase reorganization energy, which further enhances internal conversion and suppresses radiative emission, thereby quenching fluorescence (ACQ effect).[33–35] This effect clearly indicates a significant difference in reorganization energy and excited state planarity relaxation in solvent from solid in **PhPI**.

Furthermore, the **RPI**s showed low Φ_{PL} (0.03–0.2) at 99% f_w due to ACQ or NIR characteristics that are responsible for the non-radiative decay process (Fig. S12, S13, Table 1 and eqn (S1)). **DMPI**/**TPPI**/**BPPI** demonstrated 22/11/10 nm blue shifted $\lambda_{ab,max}$ in f_{Hex} (99% hexane in $CHCl_3$) (Fig. S6, S7 and Table S9). However, concentration-dependent $\lambda_{ab,max}$ of **DMPI**/**TPPI**/**BPPI** exhibited 3/2/1 nm red-shifted $\lambda_{ab,max}$ (J-type aggregation) (Fig. S8 and Table S10). At 0% f_{Hex}, **DMPI**/**TPPI**/**BPPI** revealed corresponding $\lambda_{em,max}$ at 676/657/657 nm, followed by blue shifted $\lambda_{em,max}$ enhancement at 570 nm in 99% f_{Hex}, though $\lambda_{ab,max}$/$\lambda_{em,max}$ shifts were less pronounced for **TPPI**/**BPPI** at 0% f_{Hex} due to reduced π-delocalization (showed similar characteristics with f_w) (Fig. S9). Moreover, **DMPI**/**TPPI**/**BPPI** exhibited 123/130/134 nm hydrodynamic radii that are suitable for biomedical applications (Fig. S10).

EEM spectra

Excitation Emission Matrices (EEMs) are widely applied in systems requiring multi-component analysis, as they capture unique spectral signatures that are often referred to as molecular fingerprints for complex mixtures. In the present study, 3D EEM spectral scans were recorded for the representative **RPI**s over a concentration range of 100 μM–1 mM, revealing distinct fluorophore behaviors associated with each system (Fig. 4).[36] At lower concentrations (100–500 μM), **PhPI**/**ANPI** predominantly exhibited a single emissive species, consistent with the presence of isolated fluorophores, whereas **DMPI**/**TPPI**/**BPPI** displayed dual fluorophore contributions. Thus, time-resolved photoluminescence (TRPL) measurements were performed, and the decay profiles were well fitted using a single-exponential function, which describes the relaxation of an isolated population of excited fluorophores according to eqn (1):

$$f(t) \equiv I(t)/I(0) = \exp(-t/\tau_D), \quad (1)$$

where $I(0)$ is the initial emission intensity determined by the concentration of excited donors, and τ_D represents the intrinsic excited state lifetime of the fluorophore (*i.e.*, the inverse of the spontaneous emission rate constant). The observation of single-exponential fluorescence decay indicates the presence of a single dominant emissive species and confirms that emission originates from a well-defined excited state without significant contribution from multiple emissive pathways or heterogeneous emissive environments. Notably, for **PhPI** and **ANPI**, the fluorescence lifetimes show only negligible variation with concentration, suggesting that excited state relaxation converges into a single emissive state and that radiative decay proceeds through a unique fluorophoric pathway. Such behavior is consistent with systems in which aggregation does not introduce additional emissive traps or excimer-like species (Fig. S14).[37–39] Notably, **TPPI**'s intrinsic fluorophore was essentially non-emissive at these low concentrations, indicating its weak radiative decay under dilute conditions. Upon increasing the concentration, clear trends in spectral broadening and wavelength shifts emerged. **PhPI**/**DMPI** exhibited progressively broadened spectra, suggesting concentration-driven intermolecular interactions and aggregation. By contrast, **ANPI** retained a more symmetric profile with a pronounced blue shift in λ_{ex}, indicative of reduced conjugation. At 1 mM, the behavior diverged more prominently: **DMPI**/**TPPI**/**BPPI** all developed asymmetric emission features with λ_{ex} undergoing a distinct red-shift. In particular, **TPPI** displayed a dramatic enhancement in fluorophore intensity, surpassing that of the other **RPI**s, consistent with the activation of its otherwise quenched emissive unit under high concentration conditions. The contour plots further clarified these effects: red-shifted λ_{ex} correlated with extended π-conjugation and stronger intermolecular electronic coupling, while blue shifted λ_{ex} signal decreased conjugation or enhanced steric disruption of delocalization.[36,40] Collectively, these observations indicate that the photophysical responses of the **RPI**s are strongly modulated by concentration-dependent aggregation, conjugation, and steric constraints imposed by pendant functional groups. Such effects govern the balance between emissive and non-emissive states, ultimately dictating the spectral fingerprints captured in EEM analyses.

Electronic properties

DFT analysis (B3LYP/6-31G (d, p)) revealed decreasing HOMO–LUMO gaps (E_g) with stronger donor units in the **RPI**s (Fig. 5, S15–S18 and Table 1): **PhPI** (2.660 eV) > **ANPI** (2.566) > **DMPI** (2.480) > **TPPI** (2.410) > **BPPI** (2.340 eV) (Fig. 5 and Table 1). LUMOs were confined to the **PI** core, while HOMOs extended over donor units, indicating strong push–pull interactions and enhanced π-conjugation, especially in **DMPI**/**TPPI**/**BPPI**. This correlated with red-shifted $\lambda_{abs,max}$ and far-red/NIR $\lambda_{em,max}$. However, **TPPI**/**BPPI** showed slightly reduced π-delocalization, leading to less pronounced or blue shifted $\lambda_{abs,max}$/$\lambda_{em,max}$/Stokes shifts at their dispersed state. E_g decreased more in polar solvents (DMSO/water) than in nonpolar ones ($CHCl_3$/hexane), which also showed blue shifted $\lambda_{em,max}$ in hexane due to reduced π-conjugation (Fig. S15–S18).[41,42]

Theoretical calculation

Increasing the donor unit leads to reduced E_g in **DMPI**/**TPPI**/**BPPI** (2.480/2.410/2.340 eV), which aligns well with their optical behavior (Fig. S19 and Tables 1, S11–S13).[12,43,44] These derivatives exhibited small $\Delta E_{S_1-T_1}$ of 0.623/0.639/0.522 eV, comprising significant SOC ($\zeta(S_1, T_1)$: 0.447/0.141/0.141 cm^{-1}) that enabled efficient S_1–T_1 transitions. In contrast, although **PhPI**/**ANPI** showed 0 cm^{-1} ζ (S_1, T_1), which leads to favor the S_1–T_1 transitions, yet they displayed prominent ζ (S_2, T_2) of 3.714/

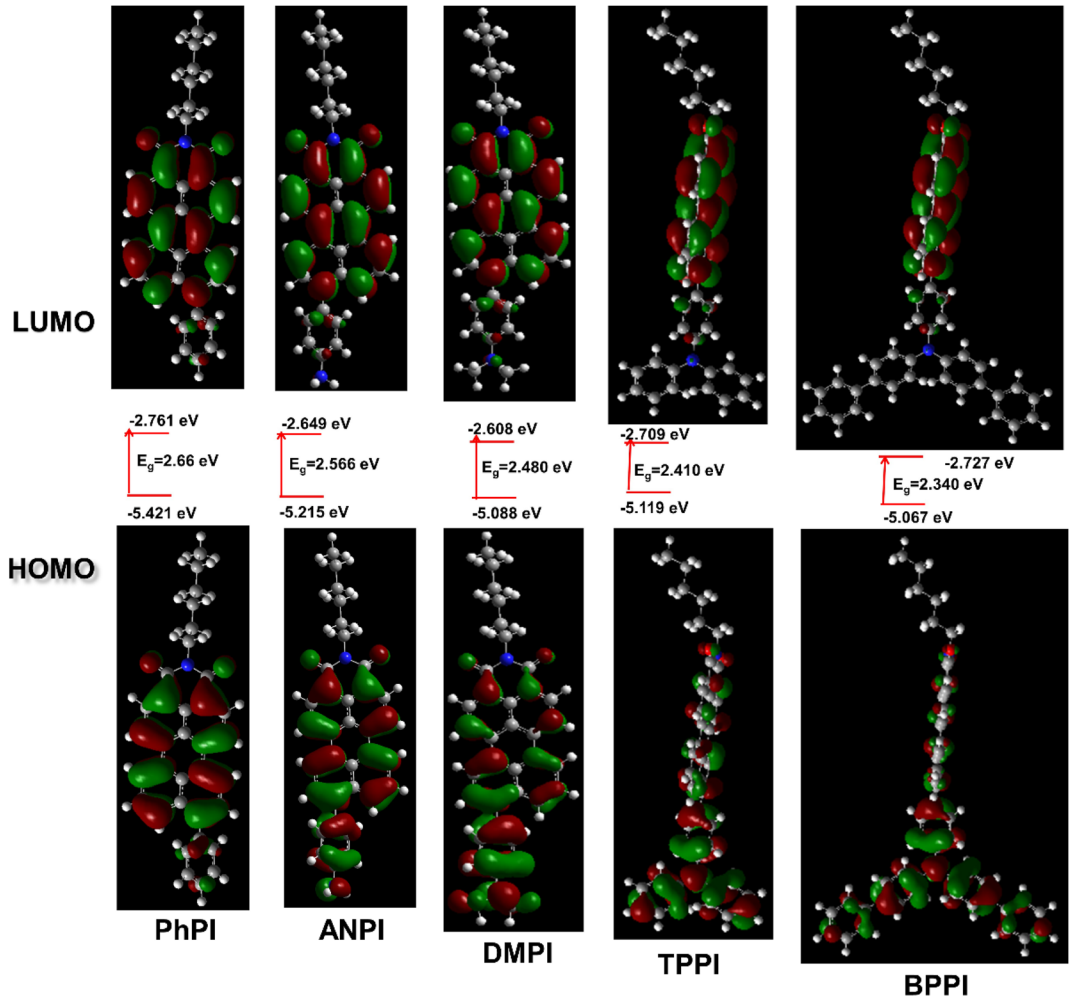

Fig. 5 Optimized ground state band energies (S_0) in eV of the RPIs in the gaseous state, calculated using DFT/B3LYP with the 6-31G (d, p) basis set (Gaussian 16).

0.435 cm^{-1}, containing a lower $\Delta E_{S_2-T_2}$ of 0.347/0.312 eV. **DMPI**/**TPPI**/**BPPI** also showed notable ζ (S_2, T_2) of 0.700/0.282/0.387 cm^{-1} with $\Delta E_{S_2-T_2}$ of 0.637/0.628/0.703 eV, respectively. Thus, **DMPI**/**TPPI**/**BPPI** confirmed favorable ISC characteristics for PS properties.

Singlet oxygen (type-II ROS) detection

Due to the substantial SOC and high T_1 population in the **RPI**s, Φ_Δ was evaluated using 9,10-anthracenediyl-bis(methylene) dimalonic acid (ABDA) in 99% f_{PBS} (99% PBS in DMSO) under white light irradiation (Fig. 6a, S20, S21, S22a, Tables 1, S14 and eqn (S2)). **TPPI** showed the highest Φ_Δ of 0.592 (type-II), while **BPPI** had a moderate Φ_Δ of 0.025. Other **RPIs** *viz.* **PhPI**/**ANPI**/**DMPI** demonstrated no detectable $^1O_2$ generation. Notably, **TPPI** exhibited a high Φ_Δ in aqueous media, though higher values (0.91/1.0/1.1) were reported for MeTTPy/NI-PSs/LOCK in organic solvents (Table S14).

Total ROS generation evaluation

Total ROS generation by the **RPIs** was assessed using 2,7-dichlorodihydrofluorescein (DCFDA) under white light in f_{PBS} (Fig. 6b and S22b–d, S23). **TPPI**/**BPPI**/**DMPI** showed 130/110/30-fold PL enhancement after 30 min of white light irradiation, while only 8-fold enhancement was observed for **PhPI**/**ANPI**. **TPPI**/**BPPI**/**DMPI** induced $2.5 \times 10^5/2.0 \times 10^5/1.8 \times 10^5$ PL enhancement within 5 minutes, confirming both type-I and type-II ROS. Thus, **DMPI**/**TPPI**/**BPPI** NIR/Far-red AIEE/AIE PSs show efficient ROS generation compared to recently reported PSs (Table S2). Efficient ROS production by **TPPI**/**BPPI** is attributed to strong donor units attached to these **RPI**s, which exert promising ICT characteristics, correspondingly lowering the ΔE_{ST} (*e.g.*, **BPPI**: 0.522 eV) and enhancing T_1 population *via* ISC (Fig. S19 and Table 1).[45] **BPPI**'s low Φ_{PL} (0.03) further supports ISC-driven ROS ($O_2^{\bullet-}$) generation.[45]

Radical (type 1 ROS) detection

The free radical generation of **RPI** was studied *via* ESR using TEMP as a $^1O_2$ trap in 99% f_{PBS} under white light (Fig. 6c). Only **TPPI** showed a detectable ESR signal, confirming $^1O_2$ generation. Terephthalic acid (TA) probing revealed significant HO$^\bullet$ production only by **ANPI** (Fig. 6d).[43] These findings suggest a dominant type-I mechanism *via* $O_2^{\bullet-}$ generation through

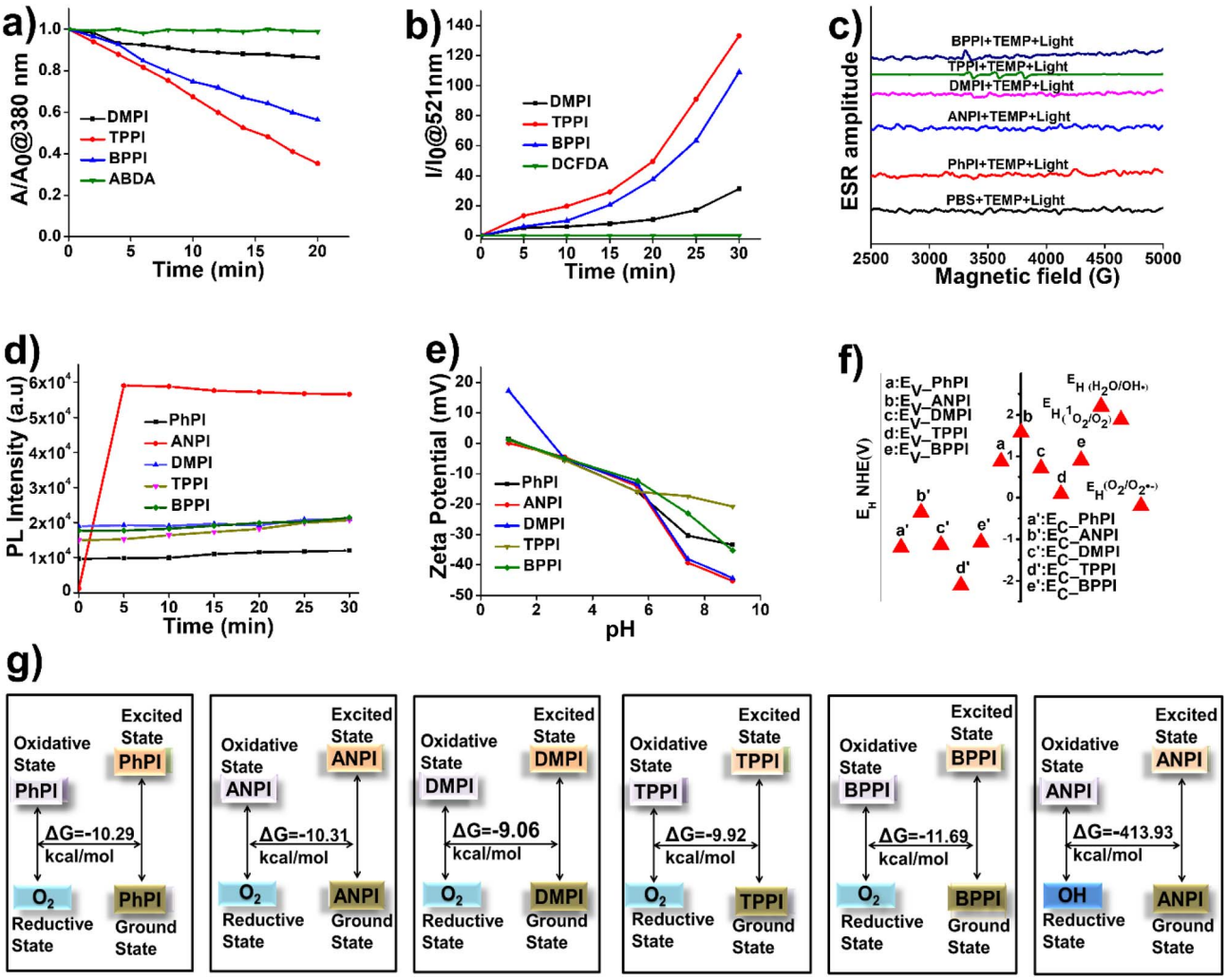

Fig. 6 (a) Plots of ABDA (100 μM) decay rates at $\lambda_{abs,max}$ of 380 nm by the different **RPI** PSs (100 μM). (b) PL plots of the DCFDA indicator in the presence of distinct **RPIs**. A_0 and A are ABDA absorbances at $\lambda_{abs,max}$ of 380 nm, whereas I_0 and I are PL of the indicator at $\lambda_{em,max}$ of 521 nm in the presence and absence of white light irradiation. (c) ESR signals in 99% f_{PBS}. (d) PL spectra of TA in the presence of the **RPIs** at 528 nm. (e) Plots of zeta potential at different pH levels of the **RPIs**. (f) E_v and E_c of the **RPIs** at pH 5.6. The energy scale is represented in relation to NHE. (g) ΔG variations of **PhPI/ANPI/DMPI/TPPI/BPPI** *via* ORCA 5.0 SOCME software at the B3LYP DEF2-SVP level.

electron transfer from T_1 to $^3O_2$. Following the reported method,[46] the points of zero zeta potential (PZZP) of the **PIs** were estimated from the zeta potential *versus* pH plots (Fig. 6e, f, S24, S25, Tables S15–S17 and eqn (S3–S6)). Initially, the aqueous solutions of the **PIs** were neutral (pH 7). Zeta potential measurements showed a transition from negative to positive values as the pH decreased from alkaline (pH 9) to acidic (pH 1). As shown in Fig. 6e, the PZZP values of **PhPI**, **ANPI**, **DMPI**, **TPPI**, and **BPPI** were 1.49, 0.103, 17.3, 1.126, and 1.23, respectively (Table S17). The valence band energy (E_v) was determined from Ultraviolet Photoelectron Spectroscopy (UPS) measurements. The conduction band energy (E_c) was estimated using the optical band gap obtained from the onset of UV-visible absorption spectra. The E_c relative to the normal hydrogen electrode (NHE) were calculated using eqn (S3) and (S4). The calculated E_v and E_c values for the **RPIs** are summarized in Table S17. Furthermore, the E_v and E_c at pH 5.6, corresponding to the PZZP, were obtained using eqn (S5) and (S6). The E_c for **PhPI/ANPI/DMPI/TPPI/BPPI** were −1.20249/−0.354323/−1.1397/−2.113966/−1.07783 eV, respectively, at pH 5.6 enabling electron transfer to $^3O_2$.[32] However, E_v for **PhPI/DMPI/TPPI/BPPI** were 1.12/0.02/0.09/1.10 eV, which are below the redox potentials for HO$^\bullet$ (2.20 eV) and $^1O_2$ (1.88 eV), making their generation unlikely – except for **TPPI** ($^1O_2$ generation explained *via* ground-triplet state energy splitting, $\Delta E_{S_0-T_1}$) and **ANPI** (HO$^\bullet$ generate due to its E_v closet to 2.20, $E_v \approx 1.90$ eV). Gibbs free energy variations (ΔG) from DFT (ORCA 5.0) indicate favorable intermolecular electron transfer (photoredox catalyst), especially for **ANPI** ($\Delta G_{OH} = -413.93$ kcal mol^{-1}), confirming its potential HO$^\bullet$ production (Fig. 6g and Tables S18–S31).[43]

Photoredox catalyst for $O_2^{\bullet-}$ generation

Light-triggered $O_2^{\bullet-}$ generation is vital for hypoxia-compatible phototherapy, as it enables $^3O_2$ on empirical data and rarely produces $O_2^{\bullet-}$ (Fig. 7).[5,8,9,43–45,47] Efficient $O_2^{\bullet-}$ generation requires rapid electron transfer from ^{3}PS* to $^3O_2$ and $\Delta E_{S_0-T_1}$

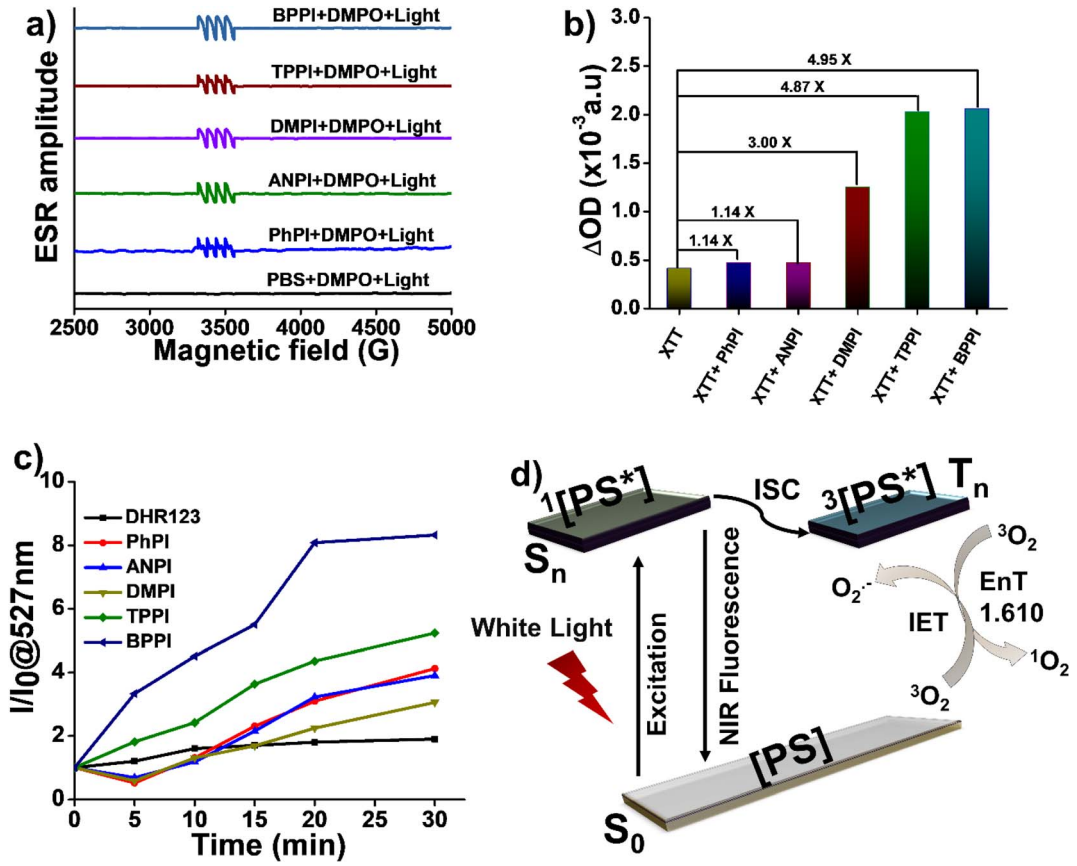

Fig. 7 (a) ESR plots of DMPO for type-I ROS $O_2^{\bullet-}$ categorization in the presence of **RPI** PSs (**PhPI**, **ANPI**, **DMPI**, **TPPI**, or **BPPI**) after 20 min of white light irradiation in dry acetonitrile solution. (b) The variation of UV-vis spectra of XTT at 470 nm after being illuminated with white light for 30 min in the presence and absence of **PhPI**, **ANPI**, **DMPI**, **TPPI**, or **BPPI** in 99% f_{PBS}. (c) DHR 123 for $O_2^{\bullet-}$ detection in the presence of **PhPI**, **ANPI**, **DMPI**, **TPPI**, or **BPPI** after white light excitation at various times in 99% f_{PBS}. (d) Schematic representation of an **RPI** to produce $O_2^{\bullet-}$ under white light excitation. [**RPI**] = 100 μM.

smaller than $^3O_2/^1O_2$ energy gap (~1.610 eV) to prevent $^1O_2$ formation (Fig. 7d).[45] Although all the **RPIs** (**PhPI**/**ANPI**/**DMPI**/**TPPI**/**BPPI**) exhibit T_1 energies (1.495/1.487/1.478/1.473/1.469 eV) above 0.98 eV, which is sufficient for $^3O_2$ sensitization, they fail to produce $^1O_2$.[48] Thus, there is an urgent need for $\Delta E_{S_0-T_1}$ calculation. **PhPI**/**ANPI**/**DMPI**/**BPPI** showed $\Delta E_{S_0-T_1}$ of 1.165/1.079/1.002/0.871 eV, which are below the 1.610 eV threshold required for $^1O_2$ generation that favors $O_2^{\bullet-}$ formation *via* ISC (Tables 1 and S32). Since type-II energy transfer requires ~94.5 kJ mol^{-1}, this becomes thermodynamically unfavorable, consisting of a smaller $\Delta E_{S_0-T_1}$.[6,45,47] **TPPI** remains an exception that generates $^1O_2$ favorably due to higher $\Delta E_{S_0-T_1}$ of 2.532 eV. These findings confirm that tuning of $\Delta E_{S_0-T_1}$ in a D-A system enables selective $O_2^{\bullet-}$ generation, supporting their role as efficient photoredox catalysts (Fig. S26).

ESR with 5,5-dimethyl-1-pyrroline-*N*-oxide (DMPO) showed six-line signals, confirming $O_2^{\bullet-}$ adducts (Fig. 7a).[45,47–49] 2,3-Bis(2-methoxy-4-nitro-5-sulfophenyl)-2*H*-tetrazolium-5-carboxanilide (XTT) assays revealed increased 470 nm absorption upon irradiation (Fig. 7b and S27), while the PL of dihydro rhodamine 123 (DHR123) at 527 nm confirmed $O_2^{\bullet-}$ production (Fig. 7c and S28).[5,8,46,49] After 30 min of light exposure, the PL increased for **PhPI**/**ANPI**/**DMPI**/**TPPI**/**BPPI** by 3/3/2/4/8-fold, validating efficient $O_2^{\bullet-}$ generation by these **RPI** photoredox catalysts (Fig. 7d).

White light-induced phototherapy performances

DMPI/**TPPI**/**BPPI** demonstrated efficient ROS generation and photocatalytic redox activity for *in vitro* phototherapy on HeLa cells (Fig. 8a). MTT assays revealed potent photo-cytotoxicity for **TPPI** (IC_{50} = 20.5 μM) under 30 min white light illumination, with complete cell eradication at 100 μM despite slight dark toxicity. **BPPI** shows dark toxicity after 10 μM and completely eradicates the HeLa cell at 100 μM under light treatment. **DMPI** showed minimal light-induced cytotoxicity due to lower ROS output, requiring NIR activation. Furthermore, photo-irradiation experiments were performed on HeLa cells using a 20 μM concentration of the materials over different time intervals. **TPPI** exhibited the highest cell killing efficiency, reaching approximately 65%, which can be attributed to its prominent PS properties under white light irradiation (Fig. S29). In contrast, **BPPI** and **DMPI** showed significantly lower cell killing efficiency, likely due to their reduced PS activity. Moreover, field-emission scanning electron microscopy (FESEM) was performed on the primary material **TPPI** and the comparative material **ANPI** to investigate their morphological evolution

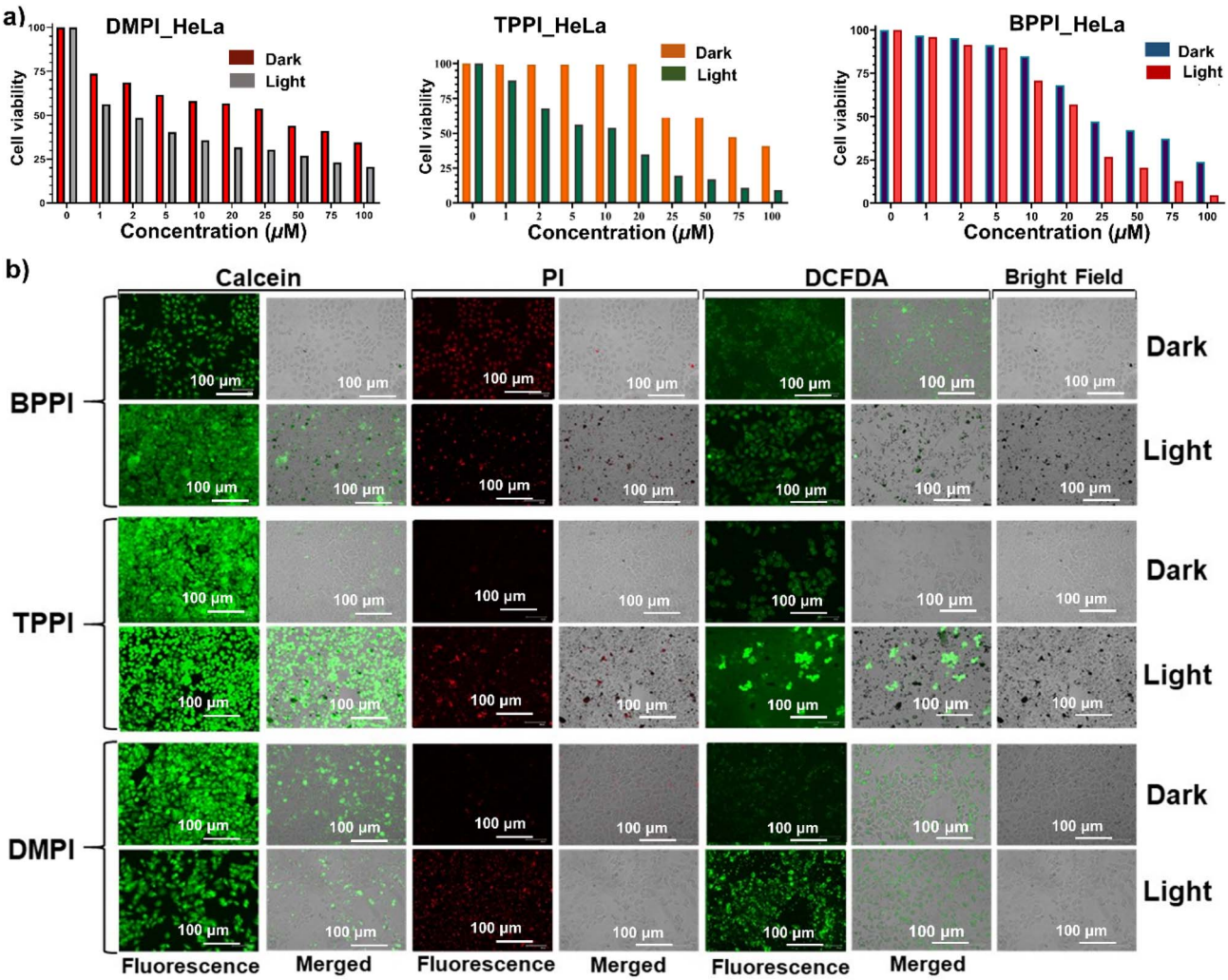

Fig. 8 (a) Cytotoxic study of HeLa cells post treatment with various concentrations of DMPI/TPPI/BPPI along with 30 min of white light illumination. Fluorescence microscope images of HeLa cells after treatment with (b) DMPI/TPPI/BPPI PSs under normoxia, loaded with PI (4 μM, dead cell marker), calcein-AM (2 μM, live cell marker), and DCFDA (10 μM, ROS indicator) [concentration: DMPI = 20 μM, TPPI = 20 μM, and BPPI = 25 μM; scale bar: 100 μm].

under light irradiation. The FESEM images reveal that **TPPI** undergoes pronounced morphology changes upon light irradiation, as evidenced by a significant reduction in particle size from approximately 200 nm to well-defined nanoparticles of about 100 nm or smaller, accompanied by a transformation from more uniform and ordered nanostructure to a irregular aggregates (Fig. S30–S33). In contrast, **ANPI** neither exhibits any notable morphological transformation nor does it show a significant change in nanoparticle sizes before and after the light irradiations. These observations provide strong visual evidence of the light responsive structural reorganization (Fig. S34 and S35). Fluorescence imaging further confirmed **TPPI**'s phototherapeutic efficacy.

Live/dead cell dual staining and intracellular ROS generation

Calcein-AM/PI staining and DCFDA imaging confirmed effective ROS generation by **TPPI** in HeLa cells under white light (Fig. 8b), with green fluorescence indicating elevated ROS levels. The treated cells showed morphological changes, such as shrinkage, reduced size, and collapse, supporting **TPPI**-induced photodynamic damage.

Plausible therapeutic mechanism of action for $O_2^{\cdot-}$ mediated phototherapy

Oxidative stress is defined as an imbalance between reactive oxygen/nitrogen species (ROS/RNS) and the cellular antioxidant defense system, which includes both enzymatic and nonenzymatic antioxidants. Sustained oxidative stress leads to biomolecular damage and contributes to various pathological conditions, including carcinogenesis and neurodegenerative disorders.[50–53] In the present study, **TPPI** induced photodynamic treatment exhibited pronounced morphological changes in HeLa cells, such as cell shrinkage, reduced cell volume, and collapse of cellular structures, indicating severe oxidative damage (Fig. 8b). This could be due to the partial O_2-recycling mode of action, allowing oxidative stress to be efficiently

triggered even at low oxygen tension, thereby promoting photodynamic damage in cancer cells.[5,45] These effects are primarily attributed to light-triggered $O_2^{\bullet-}$ generation, which subsequently participates in Fenton and Haber–Weiss reactions to yield highly reactive $^{\bullet}OH$. This cascade enables a partial O_2-recycling mechanism, allowing efficient oxidative stress induction even under low oxygen tension.[50,51] Herein, the photoexcited photosensitizer (**TPPI**) transfers an electron or proton to triplet oxygen ($^3O_2$) to generate $O_2^{\bullet-}$. The resulting $O_2^{\bullet-}$ undergoes SOD-mediated disproportionation to form H_2O_2 and regenerate $^3O_2$ (reaction 2). Subsequently, H_2O_2 reacts with Fe^{2+} *via* the Fenton reaction to produce $^{\bullet}OH$ and Fe^{3+}, while Fe^{3+} can be reduced back to Fe^{2+} by $O_2^{\bullet-}$, regenerating $^3O_2$ (reaction 3). In parallel, the Haber–Weiss reaction provides an additional pathway for $^{\bullet}OH$ production and $^3O_2$ regeneration (reaction 4). To verify this mechanism, Fenton–Haber–Weiss reactions were performed following reported protocols using **TPPI** under 30 min light irradiation, and the reaction products were analyzed by liquid chromatography-mass spectrometry (LC-MS). The enhancement of LC-mass peak of catechol at 110 [M] and 2,3-dihydroxybenzoic acid/2,5-dihydroxybenzoic acid at 155 $[M]^+$ under light irradiation, the characteristic Fenton reaction byproduct, confirms $^{\bullet}OH$ generation and which could support the occurrence of intracellular Fenton chemistry (Fig. S36 and S37). These results demonstrate that **TPPI** functions as an $O_2^{\bullet-}$ photogenerator capable of inducing oxidative stress under normoxic conditions and, importantly, that it could be effective even under hypoxic environments ($\leq$2% O_2) due to the partial O_2-recycling pathway, thereby ensuring sustained photodynamic cytotoxicity toward cancer cells.

$$\mathrm{TPPI} + {}^3O_2 \rightarrow O_2^{\bullet-} \quad (2)$$

$$O_2^{\bullet-} + H^+ \xrightarrow{SOD} H_2O_2 + {}^3O_2$$

$$H_2O_2 + Fe^{2+} \rightarrow Fe^{3+} + OH^{\bullet} + OH^-$$

$$O_2^{\bullet-} + Fe^{3+} \rightarrow Fe^{2+} + {}^3O_2 \quad (3)$$

$$O_2^{\bullet-} + H_2O_2 \rightarrow {}^3O_2 + OH^{\bullet} + OH^- \quad (4)$$

Conclusion

This study reports the careful tuning of the donor functionality in heavy-metal free PSs, with minor changes at the peri-position of the planar **PI** core, that yielded far-red/NIR (AIE/AIEE), significant Stokes shifts (213–270 nm), and exceptional (NIR AIEE/NIR) photoredox catalytic properties. The PSs **DMPI**/**BPPI** showed NIR/far-red AIEE photoredox catalytic properties for $O_2^{\bullet-}$ generation. **TPPI** showed far-red AIE/NIR dual-type PS/photoredox ($^1O_2$/$O_2^{\bullet-}$) catalytic features containing Φ_Δ of 0.59 in aqueous media, whereas **PhPI**/**ANPI** exhibited ACQ properties. **ANPI** functions as a photoredox catalyst for $^{\bullet}OH$/$O_2^{\bullet-}$ (type-I PS), comprising exceptionally low ΔG_{OH} (−413.93 kcal mol^{-1}), whereas **PhPI** was a photoredox catalyst prominently for $O_2^{\bullet-}$. Notably, this study also showed that the dimethyl-induced NIR AIEE in the planar **PI** core features very prominently among the **RPIs** which results from the steric crowding around the pendant phenyl unit, which converts **DMPI** from ACQ into AIEE form. Distinct optical properties include **DMPI**: NIR AIEE ($\lambda_{em,max}$ = 720 nm, Stokes shift = 220 nm) and NIR solid state emission ($\lambda_{em,max}$ = 770 nm, Stokes shift = 270 nm), **TPPI**: far-red AIE ($\lambda_{em,max}$ = 686 nm, Stokes shift = 175 nm) and NIR solid state emission ($\lambda_{em,max}$ = 713 nm, Stokes shift = 213 nm), and **BPPI**: far-red AIEE ($\lambda_{em,max}$ = 675 nm, Stokes shift = 186 nm) and NIR solid state emission ($\lambda_{em,max}$ = 716 nm, Stokes shift = 216 nm). The **RPIs** are engineered strategically by introducing specific electron donor subunits to reduce $\Delta E_{S_0-T_1}$, thereby hindering the efficient conversion of $^3O_2$ to $^1O_2$ that enabled efficient NIR photoredox catalytic properties. Consequently, this design principle has helped to fabricate distinct heavy-metal free (NIR AIEE/NIR) photoredox catalytic mechanisms that precisely generate $O_2^{\bullet-}$ *via* the refined $\Delta E_{S_0-T_1}$ principle. **TPPI** was engineered *via* triplet-ground-state splitting energy modulation functions through a partial O_2-recycling pathway that induces significant cancel cell death, where $O_2^{\bullet-}$ undergoes Haber–Weiss and Fenton reactions to amplify ROS generation.

Author contributions

MNK and PKI designed the experiments. MNK synthesized the materials and conducted all the characterization studies. MNK and PKI wrote and thoroughly revised the manuscript. SN carried out the *in vitro* cellular studies and fluorescence microscopic analysis. SN and SK analysed the cellular data. RDA, CS and MS performed the FESEM, TRPL and LC-MS experiments. All authors discussed the results and contributed to the manuscript.

Conflicts of interest

The authors declare no conflicts of interest.

Data availability

The data supporting this article have been included as part of the supplementary information (SI). Supplementary information: materials, instruments, synthetic procedures, and characterization data (multinuclear NMR and MALDI-TOF), as well as experimental and computational data (Schemes S1–S3, Fig. S1–S37, Tables S1–S32, and SI figures). See DOI: https://doi.org/10.1039/d5sc07763j.

Acknowledgements

The authors gratefully acknowledge financial support from the Department of Electronics & Information Technology (DeitY Project No. 5(9)/2012-NANO Vol. II), the Department of Science

and Technology (DST No. DST/SERB/EMR/2014/000034), and the DST-Max Planck Society, Germany (No. IGSTC/MPG/PG(PKI)/2011A/48). Gratitude is also extended to the Centre for Nanotechnology and the Central Instruments Facility at IIT Guwahati for instrument support, and Prof. Aditya Narayan Panda for assistance with theoretical calculations.

References

1 Y. Shen, A. J. Shuhendler, D. Ye, J.-J. Xu and H.-Y. Chen, *Chem. Soc. Rev.*, 2016, **45**, 6725–6741.
2 H. Wang, X. Yang, W. Shao, S. Chen, J. Xie, X. Zhang, J. Wang and Y. Xie, *J. Am. Chem. Soc.*, 2015, **137**, 11376–11382.
3 D. Cui, J. Huang, X. Zhen, J. Li, Y. Jiang and K. Pu, *Angew. Chem., Int. Ed.*, 2019, **58**, 5920–5924.
4 J. Li, Z. Zhuang, Z. Zhao and B. Z. Tang, *View*, 2022, **3**, 20200121.
5 M. Li, J. Xia, R. Tian, J. Wang, J. Fan, J. Du, S. Long, X. Song, J. W. Foley and X. Peng, *J. Am. Chem. Soc.*, 2018, **140**, 14851–14859.
6 R. Bonnett, *Chem. Soc. Rev.*, 1995, **24**, 19–33.
7 L. Benov, *Protoplasma*, 2001, **217**, 33–36.
8 M. Li, T. Xiong, J. Du, R. Tian, M. Xiao, L. Guo, S. Long, J. Fan, W. Sun and K. Shao, *J. Am. Chem. Soc.*, 2019, **141**, 2695–2702.
9 M. Li, Y. Shao, J. H. Kim, Z. Pu, X. Zhao, H. Huang, T. Xiong, Y. Kang, G. Li and K. Shao, *J. Am. Chem. Soc.*, 2020, **142**, 5380–5388.
10 C. Li and H. Wonneberger, *Adv. Mater.*, 2012, **24**, 613–636.
11 A. Jana, L. Bai, X. Li, H. Ågren and Y. Zhao, *ACS Appl. Mater. Interfaces*, 2016, **8**, 2336–2347.
12 W. Wu, D. Mao, F. Hu, S. Xu, C. Chen, C. J. Zhang, X. Cheng, Y. Yuan, D. Ding and D. Kong, *Adv. Mater.*, 2017, **29**, 1700548.
13 R. Docampo, S. N. Moreno, R. P. Muniz, F. S. Cruz and R. P. Mason, *Science*, 1983, **220**, 1292–1295.
14 M. N. Khatun, S. Nandy, C. Srinivas, S. Kumar and P. K. Iyer, *Adv. Opt. Mater.*, 2025, **13**, e01052.
15 J. Mei, N. L. Leung, R. T. Kwok, J. W. Lam and B. Z. Tang, *Chem. Rev.*, 2015, **115**, 11718–11940.
16 M. N. Khatun, S. Nandy, H. Roy, S. S. Ghosh, S. Kumar and P. K. Iyer, *Chem. Sci.*, 2024, **15**, 9298–9317.
17 K. Chen, R. Zhang, Z. Wang, W. Zhang and B. Z. Tang, *Adv. Opt. Mater.*, 2020, **8**, 1901433.
18 M. Jiang, X. Gu, R. T. Kwok, Y. Li, H. H. Sung, X. Zheng, Y. Zhang, J. W. Lam, I. D. Williams and X. Huang, *Adv. Funct. Mater.*, 2018, **28**, 1704589.
19 N. J. Hestand and F. C. Spano, *Chem. Rev.*, 2018, **118**, 7069–7163.
20 T.-y. Li, J. Benduhn, Z. Qiao, Y. Liu, Y. Li, R. Shivhare, F. Jaiser, P. Wang, J. Ma and O. Zeika, *J. Phys. Chem. Lett.*, 2019, **10**, 2684–2691.
21 M. Kasha, *Discuss. Faraday Soc.*, 1950, **9**, 14–19.
22 A. P. Deshmukh, N. Geue, N. C. Bradbury, T. L. Atallah, C. Chuang, M. Pengshung, J. Cao, E. M. Sletten, D. Neuhauser and J. R. Caram, *Chem. Phys. Rev.*, 2022, **3**, 021401.
23 M. Más-Montoya and R. A. Janssen, *Adv. Funct. Mater.*, 2017, **27**, 1605779.
24 W. Qin, D. Ding, J. Liu, W. Z. Yuan, Y. Hu, B. Liu and B. Z. Tang, *Adv. Funct. Mater.*, 2012, **22**, 771–779.
25 D. Ding, C. C. Goh, G. Feng, Z. Zhao, J. Liu, R. Liu, N. Tomczak, J. Geng, B. Z. Tang and L. G. Ng, *Adv. Mater.*, 2013, **25**, 6083–6088.
26 Z. Yang, W. Qin, J. W. Lam, S. Chen, H. H. Sung, I. D. Williams and B. Z. Tang, *Chem. Sci.*, 2013, **4**, 3725–3730.
27 W. Qin, K. Li, G. Feng, M. Li, Z. Yang, B. Liu and B. Z. Tang, *Adv. Funct. Mater.*, 2014, **24**, 635–643.
28 J. Wang, C. Li, Q. Chen, H. Li, L. Zhou, X. Jiang, M. Shi, P. Zhang, G. Jiang and B. Z. Tang, *Anal. Chem.*, 2019, **91**, 9388–9392.
29 L. Meng, S. Jiang, M. Song, F. Yan, W. Zhang, B. Xu and W. Tian, *ACS Appl. Mater. Interfaces*, 2020, **12**, 26842–26851.
30 M. Ojha, M. Banerjee, M. Mandal, T. Singha, S. Ray, P. K. Datta, M. Mandal, A. Anoop and N. P. Singh, *ACS Appl. Mater. Interfaces*, 2024, **16**, 21486–21497.
31 N. Meher and P. K. Iyer, *Nanoscale*, 2017, **9**, 7674–7685.
32 N. Meher and P. K. Iyer, *Nanoscale*, 2019, **11**, 13233–13242.
33 C.-C. Wu, E. Y. Li and P.-T. Chou, *Chem. Sci.*, 2022, **13**, 7181–7189.
34 S. Fatayer, B. Schuler, W. Steurer, I. Scivetti, J. Repp, L. Gross, M. Persson and G. Meyer, *Nat. Nanotechnol.*, 2018, **13**, 376–380.
35 T. Zhang, J. Zhang, F. B. Wang, H. Cao, D. Zhu, X. Chen, C. Xu, X. Yang, W. Huang and Z. Wang, *Adv. Funct. Mater.*, 2022, **32**, 2110526.
36 N. Meher, M. N. Khatun, R. Parui and P. K. Iyer, *Nanoscale*, 2025, **17**, 6685–6694.
37 E. Bodunov and A. Simões Gamboa, *J. Phys. Chem. C*, 2018, **122**, 10637–10642.
38 J. R. Martins, V. Krivenkov, C. R. Bernardo, P. Samokhvalov, I. Nabiev, Y. P. Rakovich and M. I. Vasilevskiy, *J. Phys. Chem. C*, 2022, **126**, 20480–20490.
39 C. Liu, A. Rastogi and H.-C. Yeh, *Anal. Chem.*, 2017, **89**, 4772–4775.
40 J. Dong, K. M. Solntsev and L. M. Tolbert, *J. Am. Chem. Soc.*, 2009, **131**, 662–670.
41 N. Meher, S. Panda, S. Kumar and P. K. Iyer, *Chem. Sci.*, 2018, **9**, 3978–3985.
42 N. Meher, A. P. Bidkar, D. Barman, S. S. Ghosh and P. K. Iyer, *Chem. Commun.*, 2020, **56**, 14861–14864.
43 K. Wen, H. Tan, Q. Peng, H. Chen, H. Ma, L. Wang, A. Peng, Q. Shi, X. Cai and H. Huang, *Adv. Mater.*, 2022, **34**, 2108146.
44 Z. Yang, Z. Zhang, Z. Lei, D. Wang, H. Ma and B. Z. Tang, *ACS Nano*, 2021, **15**, 7328–7339.
45 L. Yu, Y. Xu, Z. Pu, H. Kang, M. Li, J. L. Sessler and J. S. Kim, *J. Am. Chem. Soc.*, 2022, **144**, 11326–11337.
46 Y. Li, W. Zhang, J. Niu and Y. Chen, *ACS Nano*, 2012, **6**, 5164–5173.
47 K. X. Teng, W. K. Chen, L. Y. Niu, W. H. Fang, G. Cui and Q. Z. Yang, *Angew. Chem., Int. Ed.*, 2021, **60**, 19912–19920.
48 H. Bian, D. Ma, X. Zhang, K. Xin, Y. Yang, X. Peng and Y. Xiao, *Small*, 2021, **17**, 2100398.

49 P. Xiao, Z. Shen, D. Wang, Y. Pan, Y. Li, J. Gong, L. Wang, D. Wang and B. Z. Tang, *Adv. Sci.*, 2022, **9**, 2104079.
50 M. C. Catapano, M. Protti, T. Fontana, R. Mandrioli, P. Mladěnka and L. Mercolini, *Molecules*, 2019, **24**, 3066.
51 A. Rahal, A. Kumar, V. Singh, B. Yadav, R. Tiwari, S. Chakraborty and K. Dhama, *BioMed Res. Int.*, 2014, **2014**, 761264.
52 B. Giasson, J. Duda, I. Murray, Q. Chen, J. M. Souza, H. I. Hurtig, H. Ischiropoulos, J. Q. Trojanowski and V. M. Lee, *Science*, 2000, **290**, 985–989.
53 T. M. Dawson and V. L. Dawson, *Science*, 2003, **302**, 819–822.